

# Catalytic polysulfide conversion and physiochemical confinement for lithium–sulfur batteries

Sun, Zixu; Vijay, Sudarshan; Heenen, Hendrik H.; Eng, Alex Yong Sheng; Tu, Wenguang; Zhao, Yunxing; Koh, See Wee; Gao, Pingqi; Seh, Zhi Wei; Chan, Karen; Li, Hong

2020

Sun, Z., Vijay, S., Heenen, H. H., Eng, A. Y. S., Tu, W., Zhao, Y., . . . Li, H. (2020). Catalytic polysulfide conversion and physiochemical confinement for lithium–sulfur batteries. *Advanced Energy Materials*, 10(22), 1904010-. doi:10.1002/aenm.201904010

<https://hdl.handle.net/10356/142178>

<https://doi.org/10.1002/aenm.201904010>

---

This is the accepted version of the following article: Sun, Z., Vijay, S., Heenen, H. H., Eng, A. Y. S., Tu, W., Zhao, Y., . . . Li, H. (2020). Catalytic polysulfide conversion and physiochemical confinement for lithium–sulfur batteries. *Advanced Energy Materials*, 1904010-, which has been published in final form at <http://dx.doi.org/10.1002/aenm.201904010>. This article may be used for non-commercial purposes in accordance with the Wiley Self-Archiving Policy [<https://authorservices.wiley.com/authorresources/Journal-Authors/licensing/self-archiving.html>].

## Supporting Information

**Catalytic Polysulfide Conversion and Physiochemical Confinement for Lithium-Sulfur Batteries**

*Zixu Sun<sup>†1</sup>, Sudarshan Vijay<sup>†2</sup>, Hendrik Heenen<sup>†2</sup>, Alex Yong Sheng Eng<sup>3</sup>, Wenguang Tu<sup>1</sup>, Yunxing Zhao<sup>4</sup>, See Wee Koh<sup>1</sup>, Pingqi Gao<sup>5</sup>, Zhi Wei Seh<sup>3</sup>, Karen Chan<sup>\*2</sup>, Hong Li<sup>\*1,6,7</sup>*

<sup>1</sup>School of Mechanical and Aerospace Engineering, Nanyang Technological University, 639798, Singapore

<sup>2</sup>Catalysis Theory Center, Department of Physics, Technical University of Denmark, Lyngby, Denmark 2820

<sup>3</sup>Institute of Materials Research and Engineering, Agency for Science, Technology and Research (A\*STAR), 2 Fusionopolis Way, Innovis, Singapore 138634, Singapore

<sup>5</sup>Ningbo Institute of Material Technology and Engineering, Chinese Academy of Sciences, Ningbo 315201, China

<sup>4</sup>School of Materials, Sun Yat-sen University, Guangzhou 510275, China

<sup>6</sup>Centre for Micro-/Nano-electronics (NOVITAS), School of Electrical and Electronic Engineering, Nanyang Technological University, 639798, Singapore

<sup>7</sup>CINTRA CNRS/NTU/THALES, UMI 3288, Research Techno Plaza, 637553, Singapore

<sup>†</sup>equal contribution

<sup>\*</sup>corresponding authors. Karen Chan: [kchan@fysik.dtu.dk](mailto:kchan@fysik.dtu.dk); Hong Li: [ehongli@ntu.edu.sg](mailto:ehongli@ntu.edu.sg)

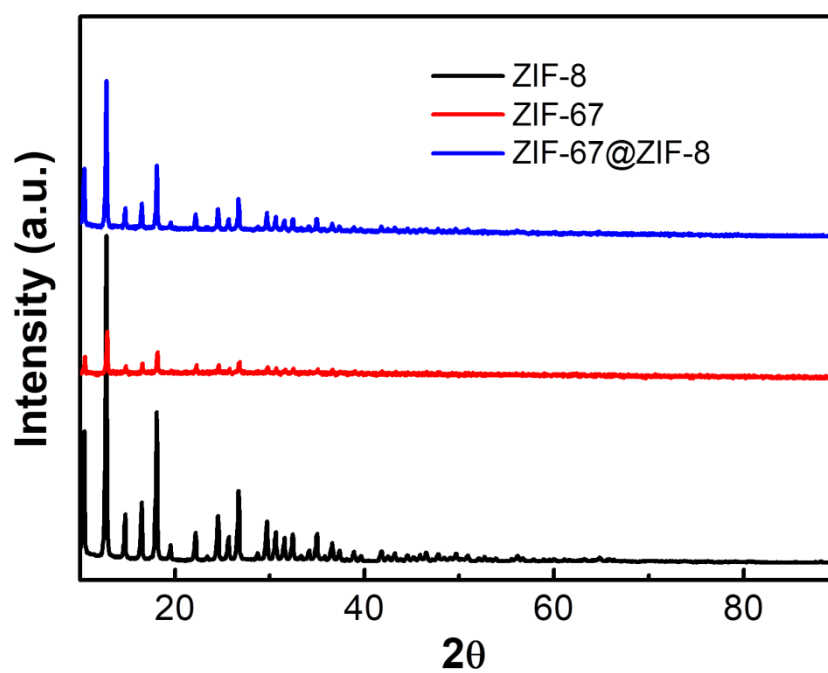


**Figure S1** XRD pattern of ZIF-8, ZIF-67, and ZIF-8@ZIF-67.

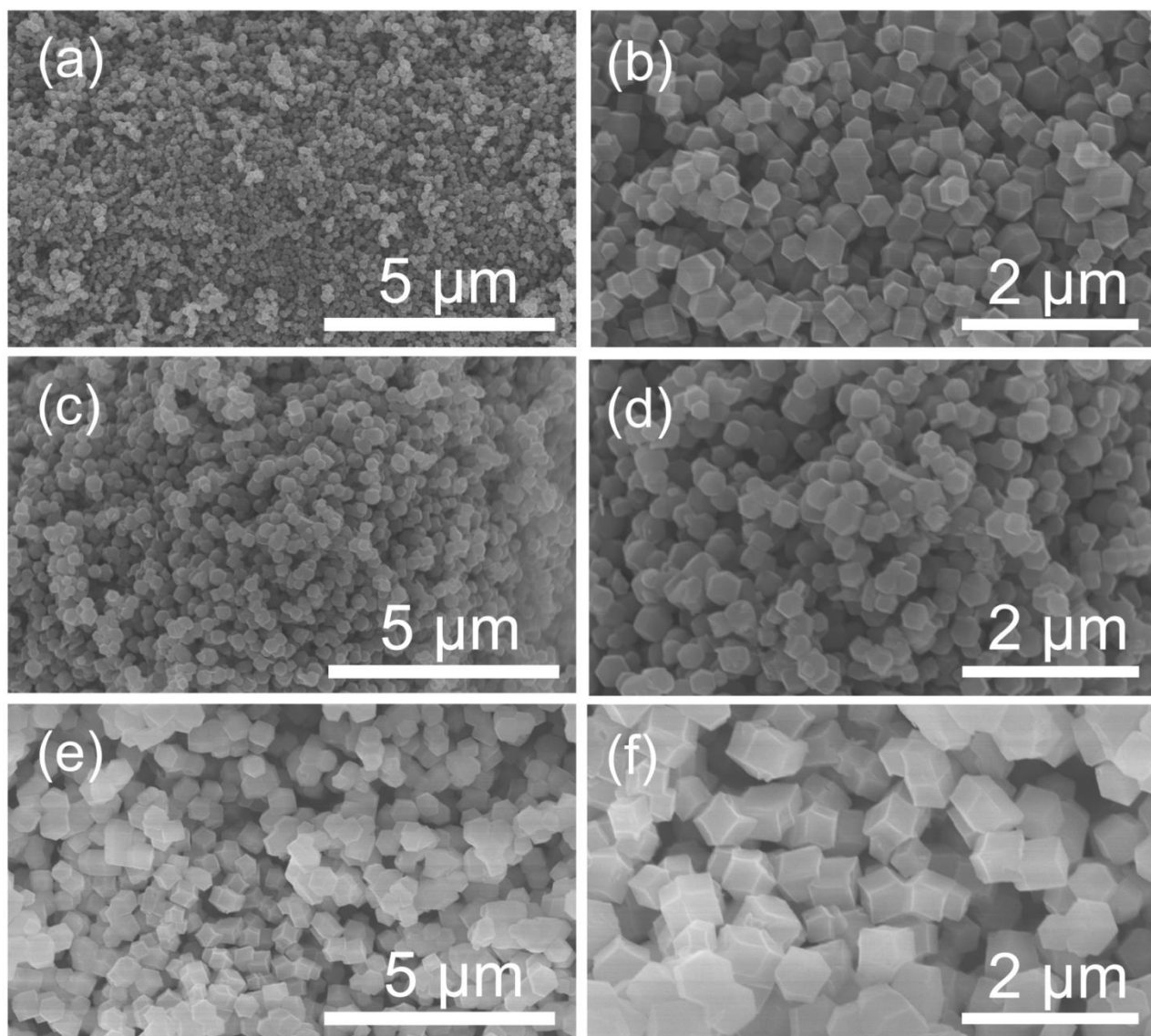


**Figure S2** Low- and high-magnification SEM images of ZIF-8 (a, b), ZIF-67 (c, d),  
and ZIF-8@ZIF-67 (e, f).

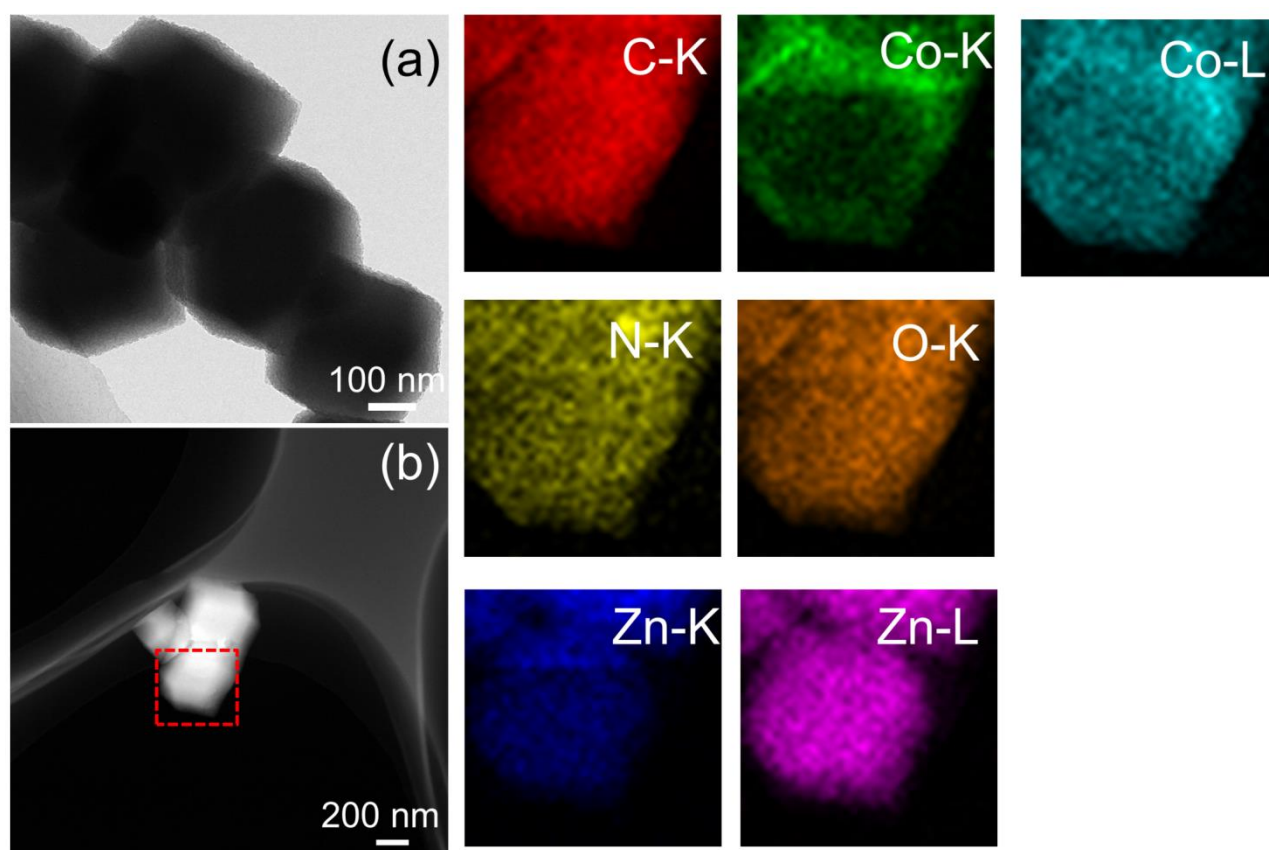


**Figure S3** (a) TEM image of ZIF-8@ZIF-67; (b) Elemental mapping of ZIF-8@ZIF-67.

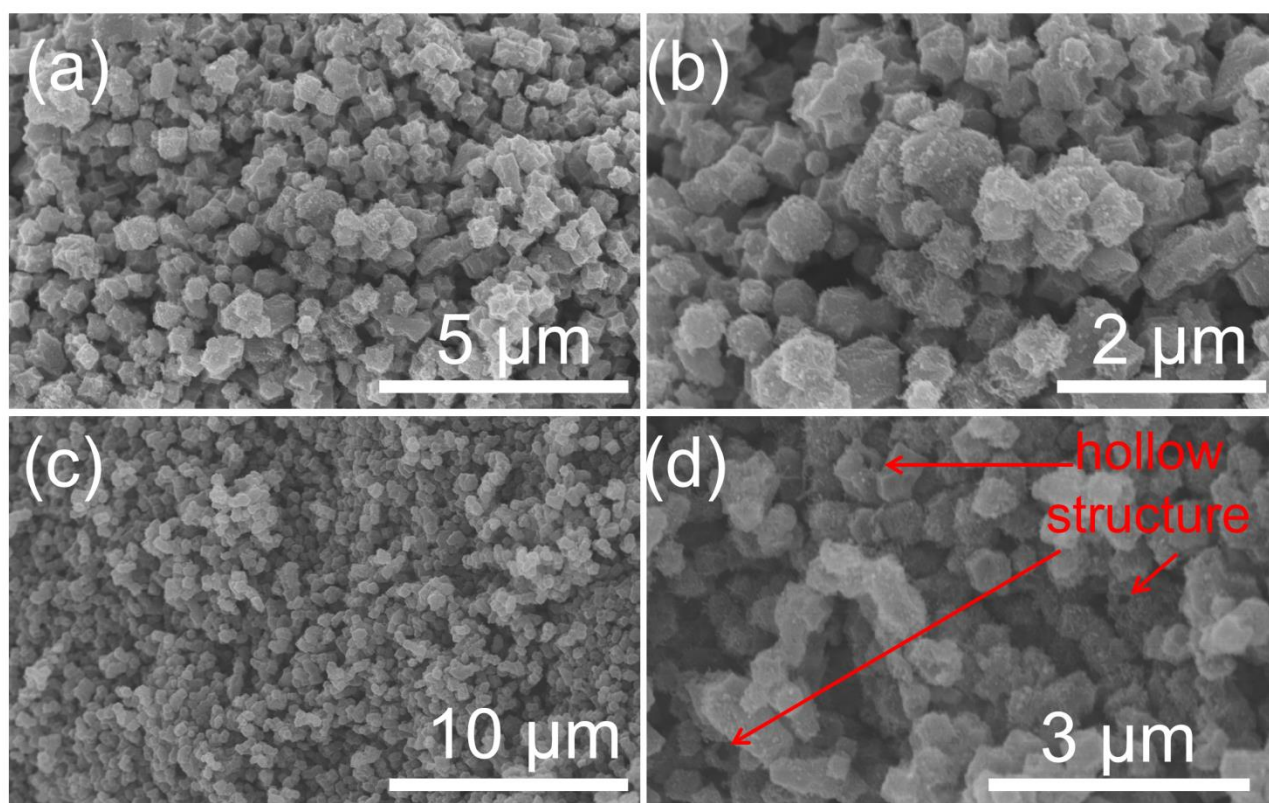


**Figure S4** Low- and high-magnification SEM images of *h*-NC (a, b). Low- and high-magnification SEM images of the as-prepared *h*-Co@NC (c, d).

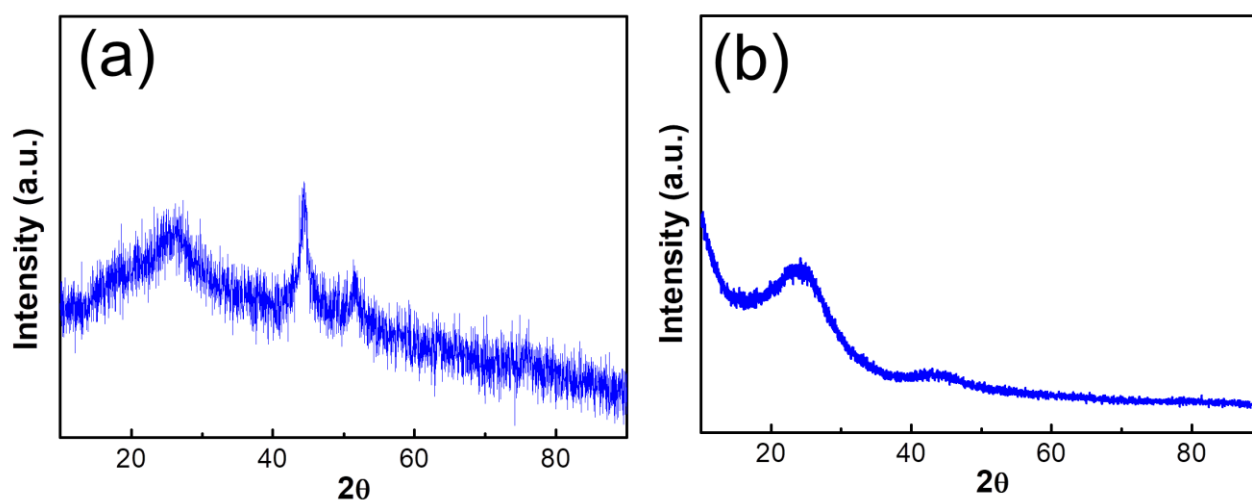


**Figure S5** XRD patterns of the  $h$ -Co@NC (a) and  $h$ -NC (b).



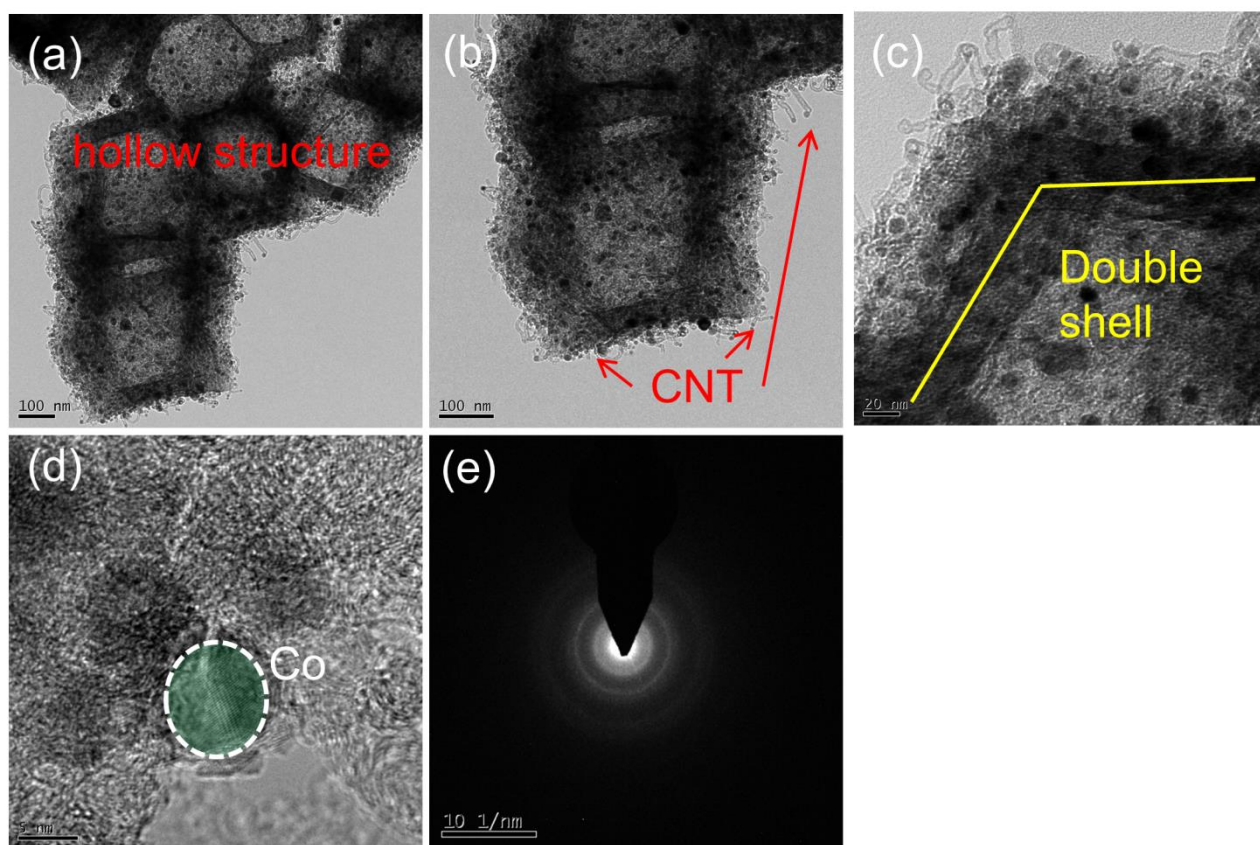


**Figure S6** (a-c) TEM images of *h*-Co@NC. (d) HRTEM image of *h*-Co@NC. (e) Selected area electron diffraction (SAED) spectroscopy.



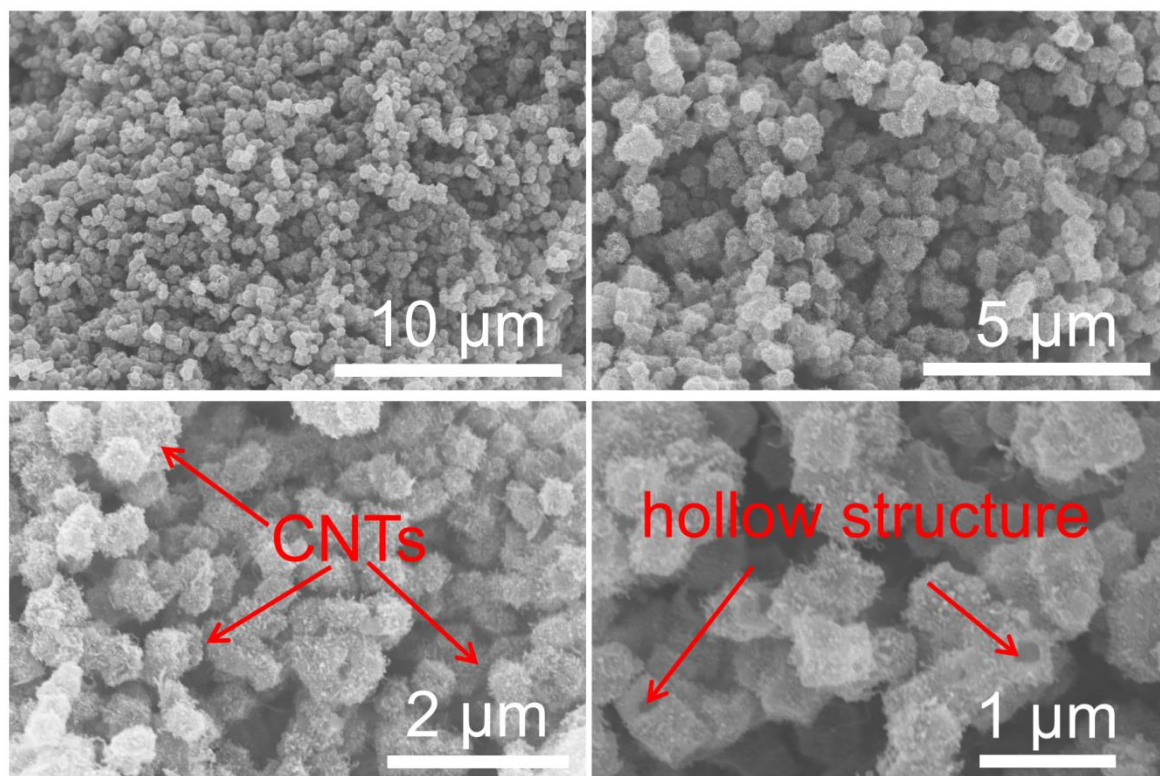


**Figure S7** Low- and high-magnification SEM images of *h*-Co<sub>4</sub>N@NC.

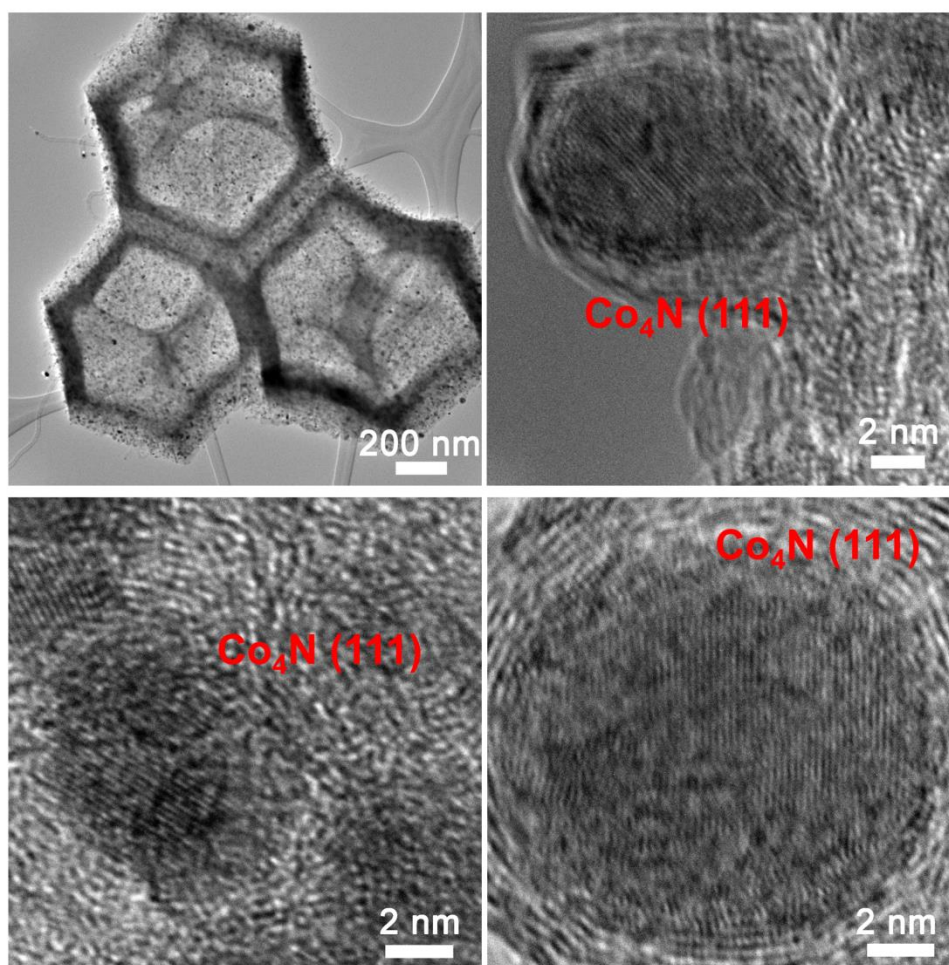


**Figure S8** TEM and high-resolution TEM images of the *h*-Co<sub>4</sub>N@NC.

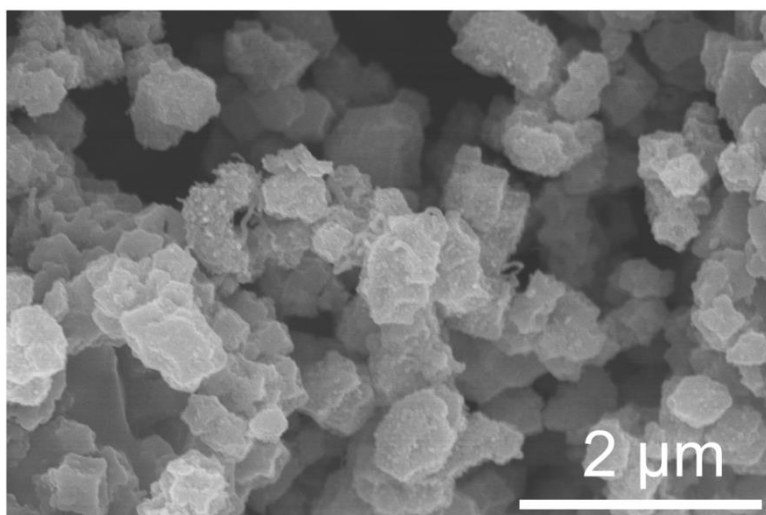


**Figure S9** SEM images of *h*-Co<sub>4</sub>N@NC/S.

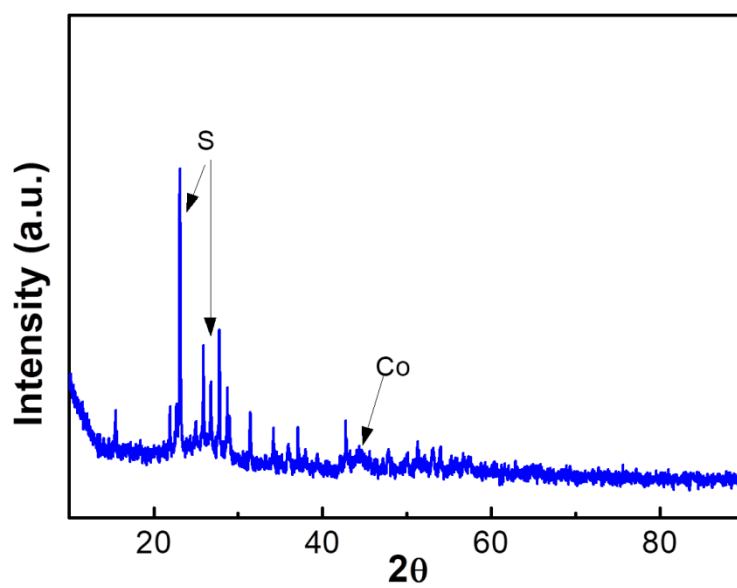


**Figure S10** XRD pattern of the *h*-Co@NC/S.

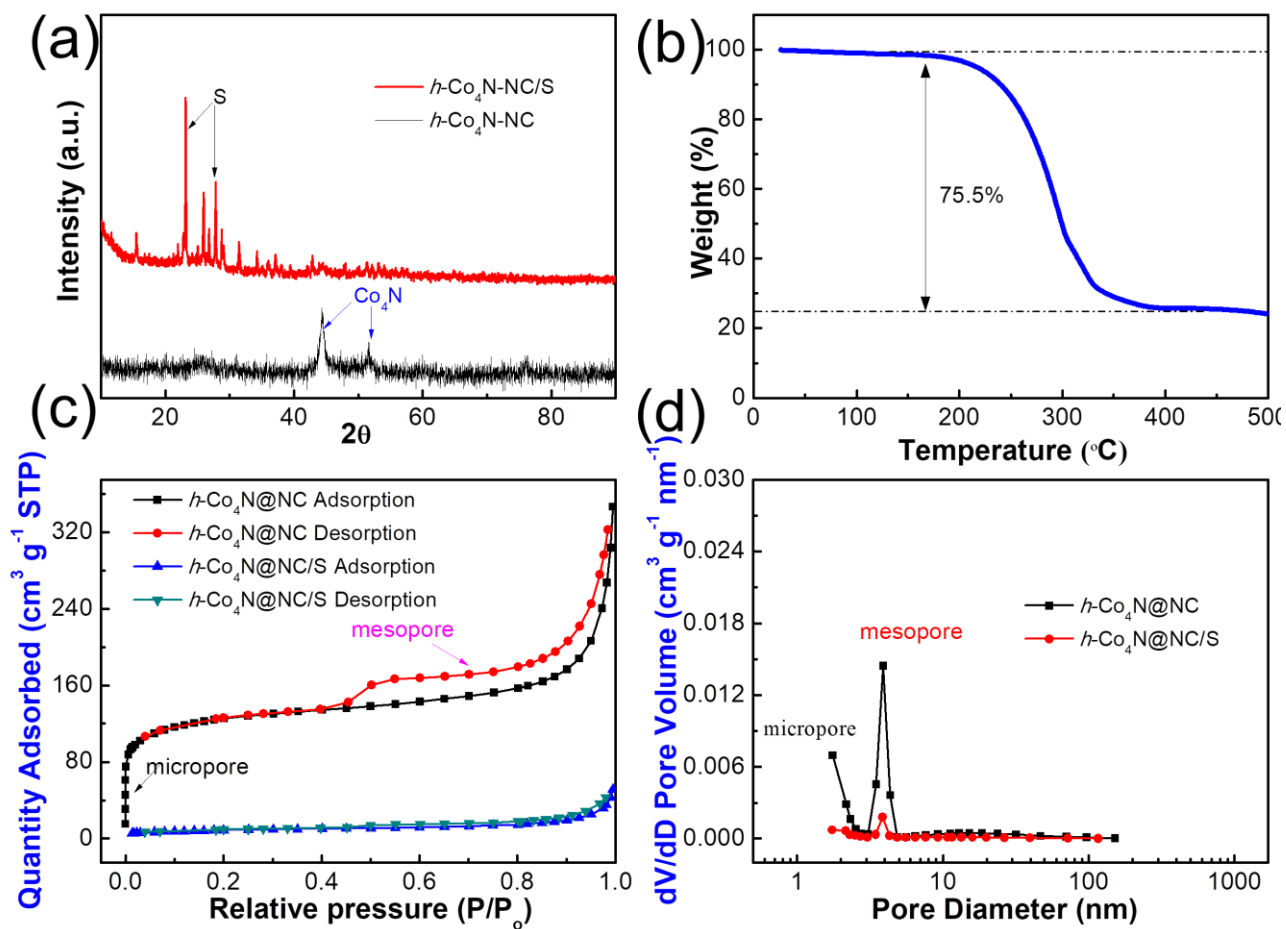


**Figure S11** (a) XRD patterns of the  $h\text{-Co}_4\text{N@NC}$  and  $h\text{-Co}_4\text{N@NC/S}$  composites. (b) TGA curve of the  $h\text{-Co}_4\text{N@NC/S}$  composites. (c) Nitrogen adsorption-desorption isotherm and (d) pore size distribution of  $h\text{-Co}_4\text{N@NC}$  and  $h\text{-Co}_4\text{N@NC/S}$ .

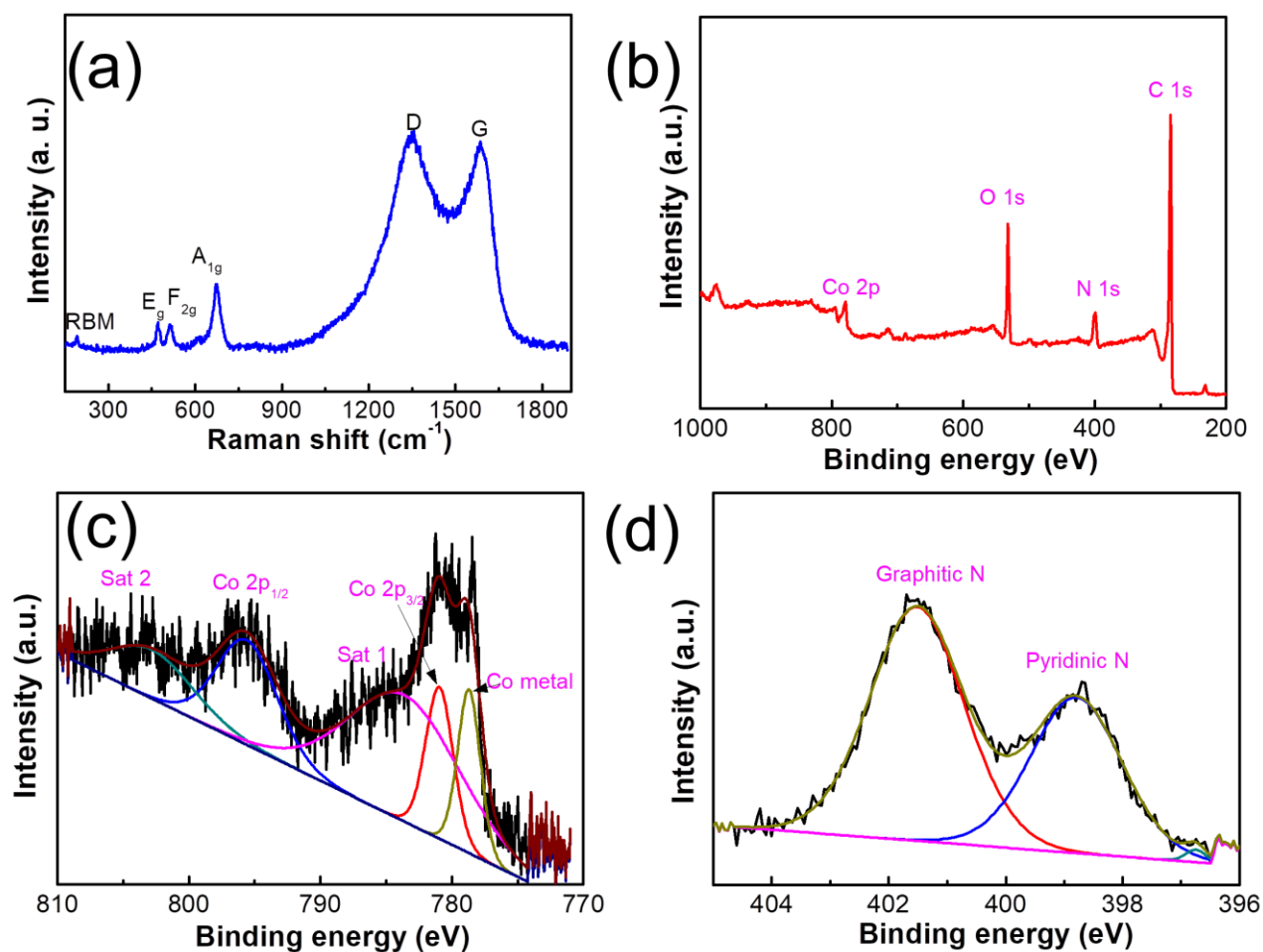


**Figure S12** (a) Raman spectrum of the  $h\text{-Co}_4\text{N@NC}$ . (b) XPS spectrum of the  $h\text{-Co}_4\text{N@NC}$ .

High-resolution XPS Co 2p (c) and N 1s (d) spectrum of  $h\text{-Co}_4\text{N@NC}$ .

**1 mM  $\text{Li}_2\text{S}_6$   
in DOL/DME**

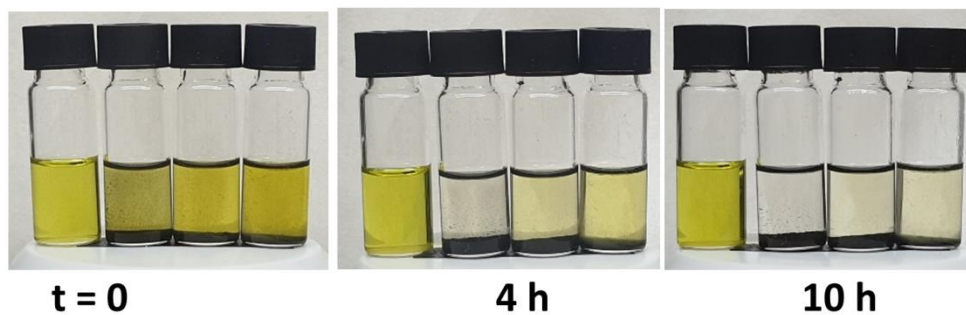


**Figure S13** Photographs of the adsorption measurement (from left to right: stock solution,  $h\text{-Co}_4\text{N@NC}$ ,  $h\text{-Co@NC}$ ,  $h\text{-NC}$  in  $\text{Li}_2\text{S}_6$  solution).

**Experimental Conditions:**

- 15 mg sample each,
- 2 mL polysulfide solution added, swirled to mix thoroughly

Solution filtered through 0.2  $\mu\text{m}$  PTFE filter before measurement



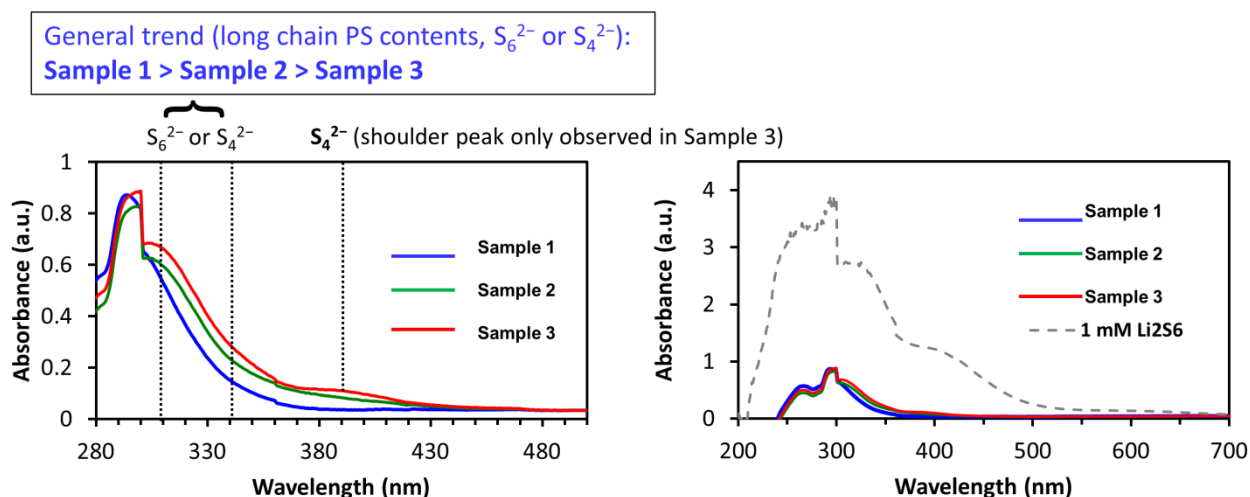


**Figure S14** UV-vis spectrum of the bare  $\text{Li}_2\text{S}_6$  solution and solutions after the adsorption test for 10 h (sample 1:  $h\text{-Co}_4\text{N@NC}$ , sample 2:  $h\text{-Co@NC}$ , and sample 3:  $h\text{-NC}$ ).

This strong chemisorption energy, in combination with Li/S diffusion from the catalyst onto the N-doped graphite may rationalize the faster intercalation in the presence of the catalyst within the 10h adsorption experiment demonstrated in **Figure S13**. The quantitative comparison for the three samples using the UV-vis spectrum of bare  $\text{Li}_2\text{S}_6$  solution and solutions after the adsorption test are characterized, as shown in **Figure S14**. The UV-vis spectra of the solution with added  $h\text{-Co}_4\text{N@NC}$  after the adsorption test show the most removal tendency, which demonstrates the  $h\text{-Co}_4\text{N@NC}$  sample shows the best adsorption capacity.

**Theory details SI:****Determination of relevant Co<sub>4</sub>N surfaces**

Co<sub>4</sub>N surfaces energies were determined for the low Miller index surfaces (100), (111), (110), and (211) as shown in table Sx1. The surface energies were calculated via  $E_{\text{surf}} = \frac{1}{2A}(E_{\text{slab}} - N_{\text{bulk}}E_{\text{bulk}})$  where  $E_{\text{bulk}}$  is the energy of the bulk unit cell,  $A$  is the surface area,  $E_{\text{slab}}$  the energy, and  $N_{\text{bulk}}$  the number of bulk units in each respective surface slab model. 1x1 slab models with a vacuum separation of 15 Å were employed. Surface energies converged at a slab-thickness of 8 layers as shown in **table S1**. To maintain the stoichiometry all slab models included both possible surface terminations: a Co-only and a Co/N terminated surface. Both terminations were considered in the sampling procedures for S and S/Li coverage described below.

**Table S1** Surface energies in eV/Å for different surface models of Co<sub>4</sub>N. The surface energies are also shown for different number of layers considered in the slab model.

Co <sub>4</sub> N surface	4-layers	8-layers	12-layers
(100)	0.091	0.093	0.092
(111)	0.100	0.099	0.099
(110)	0.108	0.108	0.107
(211)	0.109	0.109	0.109

**Sampling of Li/S coverage**

The S and mixed Li/S coverage of the Co(101), Co<sub>4</sub>N(100), and Co<sub>4</sub>N(111) surfaces were systematically sampled. All attempts to physisorb S<sub>8</sub> rings on any of the atomistic models resulted in their dissociation to chemisorbed S species during geometry optimizations. Thus,

chemisorbed atomic S and Li species are considered in the sampling. This methodology allows for a systematic sampling in respect of surface sites as identified via the software package CatKit [10.1021/acs.jpca.9b00311] on the 1x1 Co(101), 1x1 Co<sub>4</sub>N(111) and 2x1 Co<sub>4</sub>N(100) slab models. In order to account for atomic relaxation, each considered surface configurations was subjected to a geometry optimization. To minimize computational cost some constraints were used for the surface sampling:

- i. The sampling of the lithiation of S covered surfaces was only conducted for the most favorable S loading which we considered as predominant on the Co and Co<sub>4</sub>N surfaces. For every surface this loading was found to be 2 S atoms per slab model.
- ii. A cutoff for adsorbate distances was used to rule out improbable structures. When sampling the S coverage, structures with S-S distances  $< 2.5 \text{ \AA}$  for the two S case and  $< 2.0 \text{ \AA}$  for the three and four S case were discarded. For the case of Li coverage sampling structures with Li-S, Li-Li distances of  $< 1.5, 2 \text{ \AA}$  were excluded. All cut-offs were chosen based on an initial random sampling of several surface configurations were all shorter distances relaxed beyond these distances. Very few of the subsequent geometry optimizations relaxed to shorter distances. Corresponding final structures are energetically unfavorable, confirming this distance cutoff approximation (see **Figure S15**).
- iii. If the number of remaining configurations exceeded 50 configurations, the subsamples were randomly chosen. In order to include most diverse structures, the structures were binned based on the internal adsorbate-adsorbate distances. From each bin a representative subsample was randomly chosen. To remain representative, 30% of configurations were considered in the subsamples.

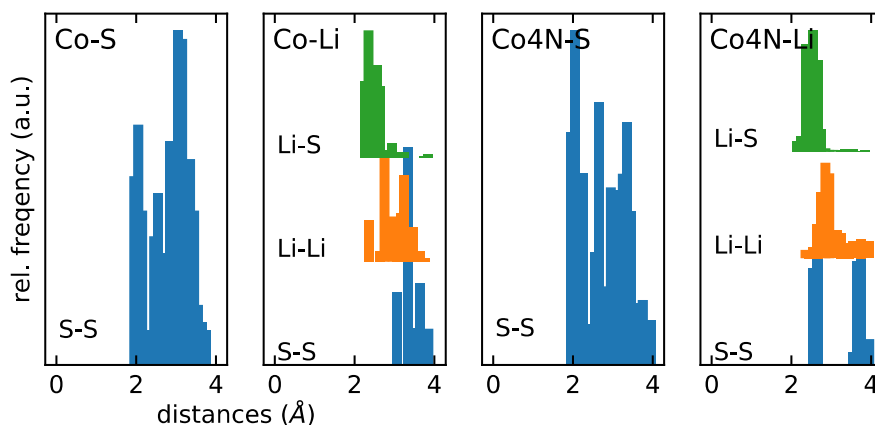


**Figure S15** Normalized histograms of S-S, Li-Li, and Li-S distances found in all optimized structures for the S- and Li-sampling in Co(101) slabs (first and second left) and S- and Li-sampling in Co<sub>4</sub>N slabs (second-last and last right).

In total 404 configurations were sampled to determine the convex hull for S coverages and 188 configurations for the Li coverages. The convex-hull plots for the different surface loadings are shown in Figure 4 in the main text for S and in **Figure S16** for Li.

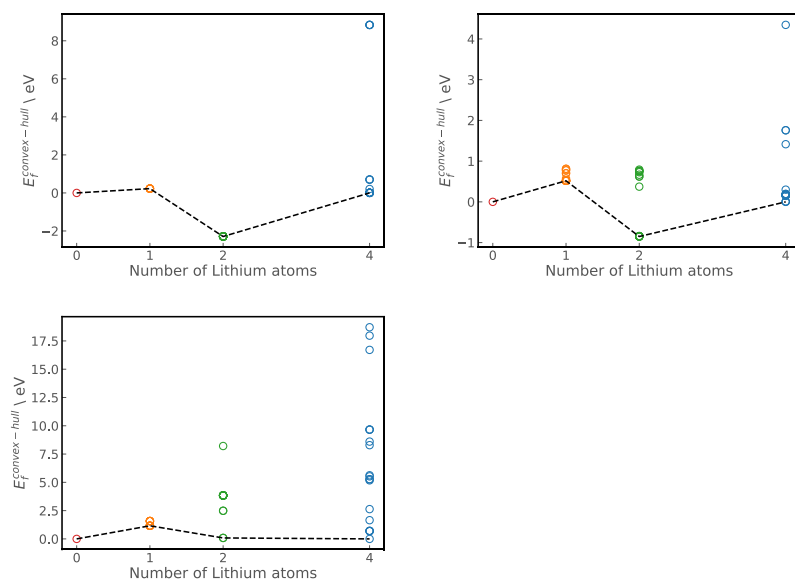


**Figure S16** Convex hull depiction for different Li loadings on the Co(101) (left), Co<sub>4</sub>N(100) (center), and Co<sub>4</sub>N(111) (right) surface covered with two S atoms.

## Electronic conductivity of S covered Co and Co<sub>4</sub>N surfaces

The density of states (DOS) is shown for clean and S covered Co(101) and Co<sub>4</sub>N(111) in **Figure S17** and **S18**, respectively. The S covered models correspond to the most stable configurations of the most stable S loading (of S=2) as described above. It can be seen, that all slab models exhibit a metallic character confirming their electronic conductivity.

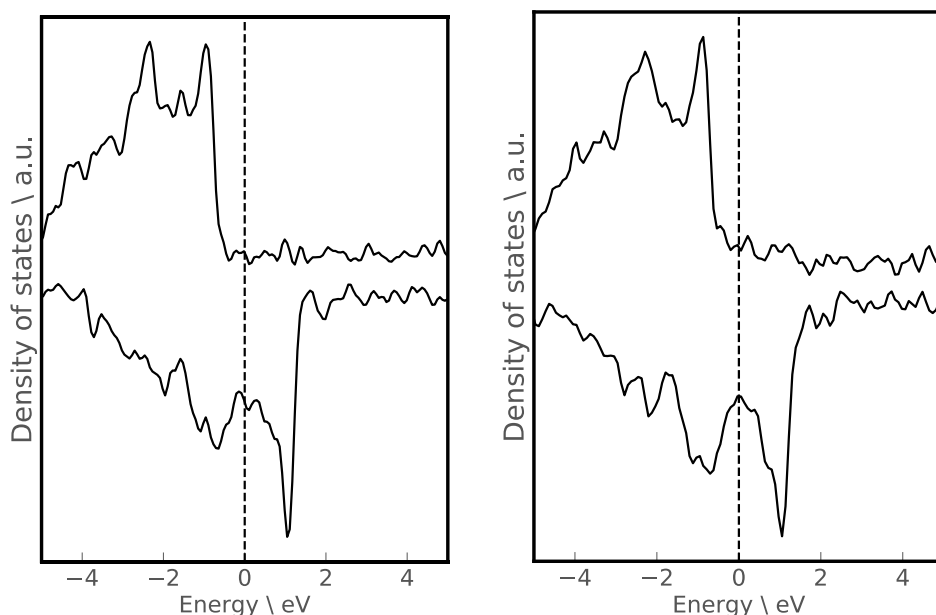


**Figure S17** DOS plots for the clean (left) and S covered (right) Co(101) surface. The most stable S-covered configuration is shown. The upper and lower line in each plot corresponds to the spin-up and spin-down spin-density.

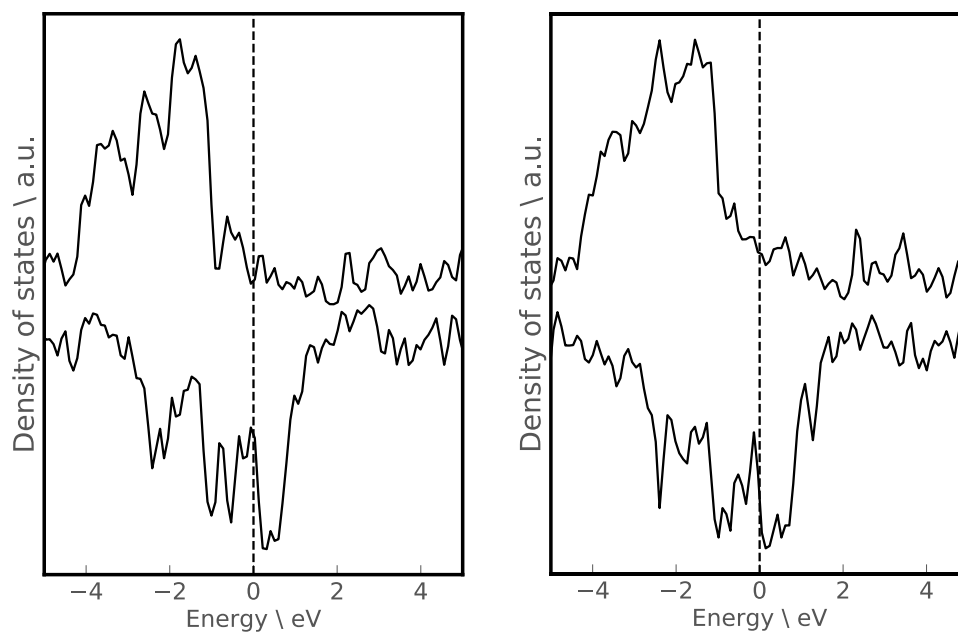


**Figure S18** DOS plots for the clean (left) and S covered (right) Co<sub>4</sub>N(111) surface. The most stable S-covered configuration is shown. The upper and lower line in each plot corresponds to the spin-up and spin-down spin-density.

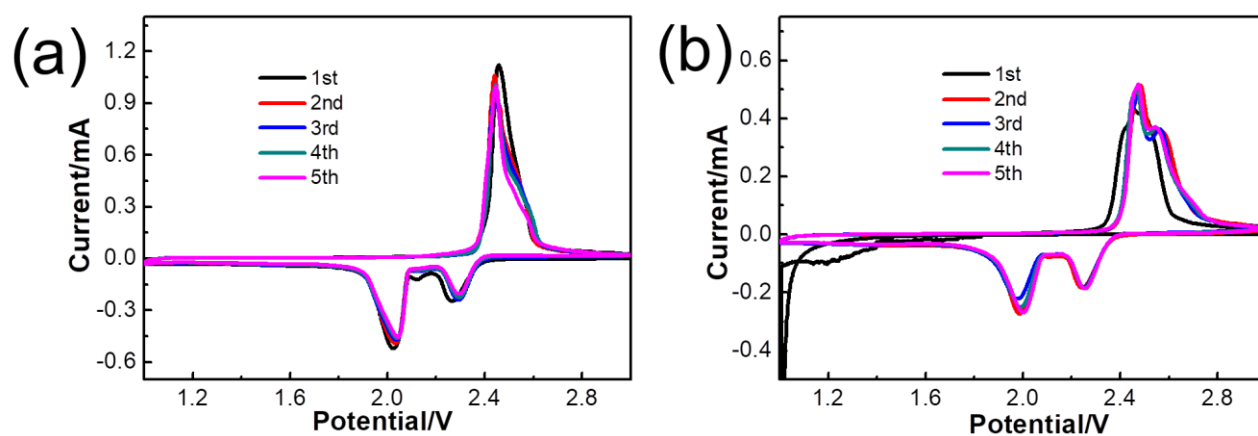


**Figure S19** (a) CV curves of *h*-Co@NC/S (b) and *h*-NC/S.



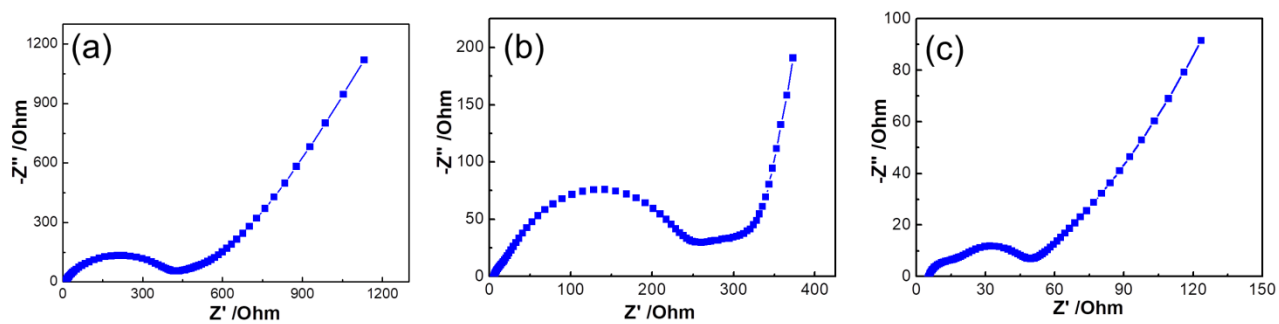


**Figure S20** Nyquist plots of the *h*-Co@NC/S (a), *h*-NC/S (b) and (c) *h*-Co<sub>4</sub>N@NC/S electrodes after the first cycles.

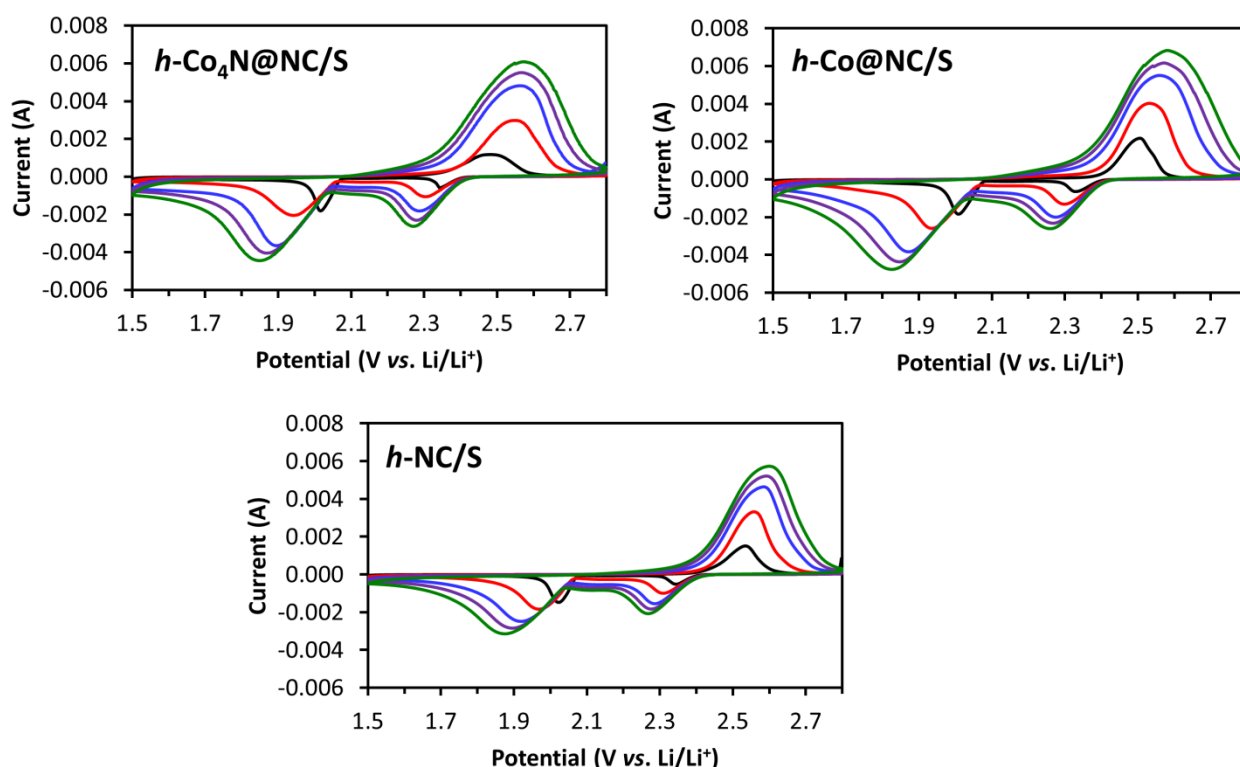


**Figure S21** CV curves of the *h*-Co<sub>4</sub>N@NC/S, *h*-Co@NC/S and *h*-NC/S electrode.

Experimental condition: cathode area: 1 cm<sup>2</sup>; Scan rate: 0.1, 0.3, 0.6, 0.8 and 1.0 mV/s.

#### Experimental Conditions:

- 1 M LiTFSI in DOL/DME, 3% LiNO<sub>3</sub>
- Cathode area: **1 cm<sup>2</sup>**
- Scan rate: 0.1, 0.3, 0.6, 0.8, 1.0 mV/s
- sulfur melt diffusion performed as per experimental
- Note: initial cycle at 0.1 mV/s omitted
  - subsequent cycles shown below

We do the curve fitting for the three samples to check the dynamic performance. The CV measurements were executed at different scan rates from 0.1 to 1.0 mV s<sup>-1</sup> to explore the kinetics of Li<sup>+</sup> insertion/extraction and Li<sup>+</sup> diffusion rate in the battery, as shown in **Figure S21** and **Figure S22**. All the anodic and cathodic peak currents maintain a linear relationship with the square root of scan rates. The Li<sup>+</sup> diffusion capability can be obtained using the

Randles-Sevcik equation.  $D_{\text{Li}^+}$  for the  $h\text{-Co}_4\text{N@NC}$  electrode is over 10 times higher than that of the  $h\text{-Co@NC}$  and  $h\text{-NC}$  electrodes, which demonstrates that  $\text{Li}^+$  diffusion kinetics for the  $h\text{-Co}_4\text{N@NC}$  electrode is significantly enhanced.

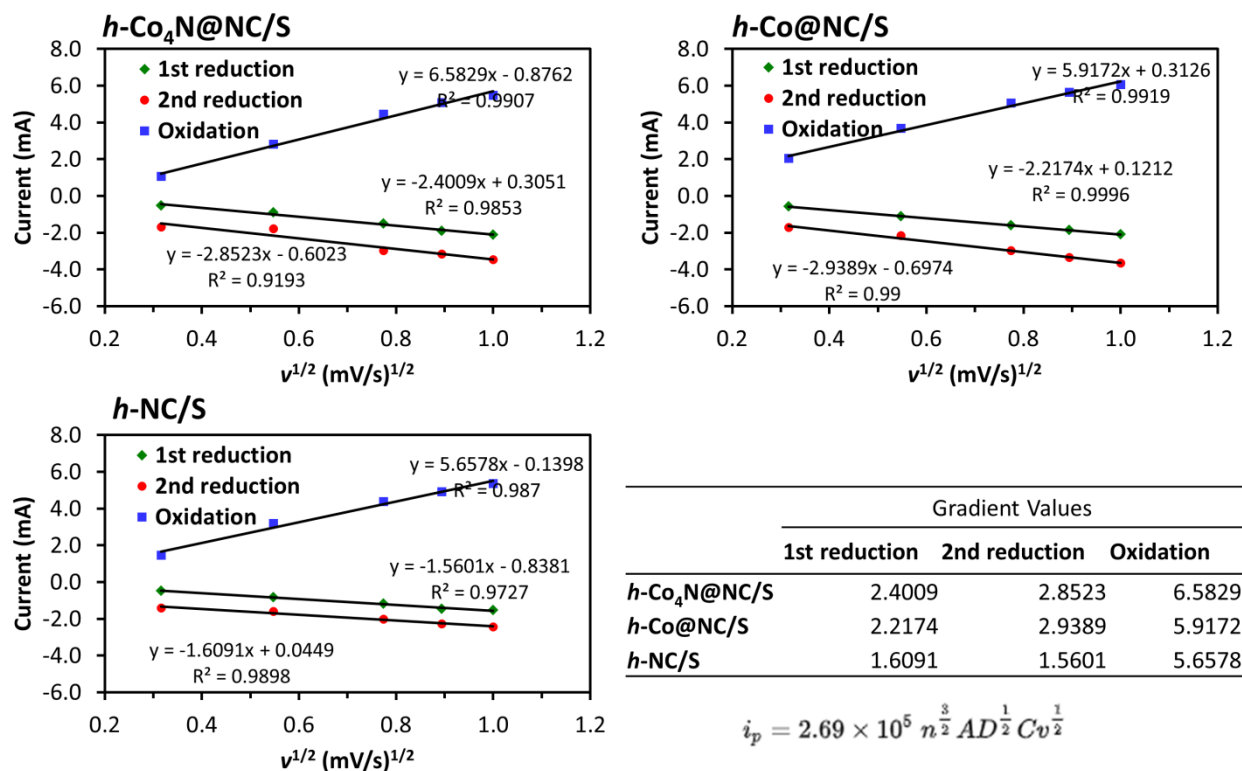


**Figure S22** Peak currents of versus square root of scan rates of the  $h\text{-Co}_4\text{N@NC/S}$ ,  $h\text{-Co/S}$  and  $h\text{-NC/S}$  electrodes.

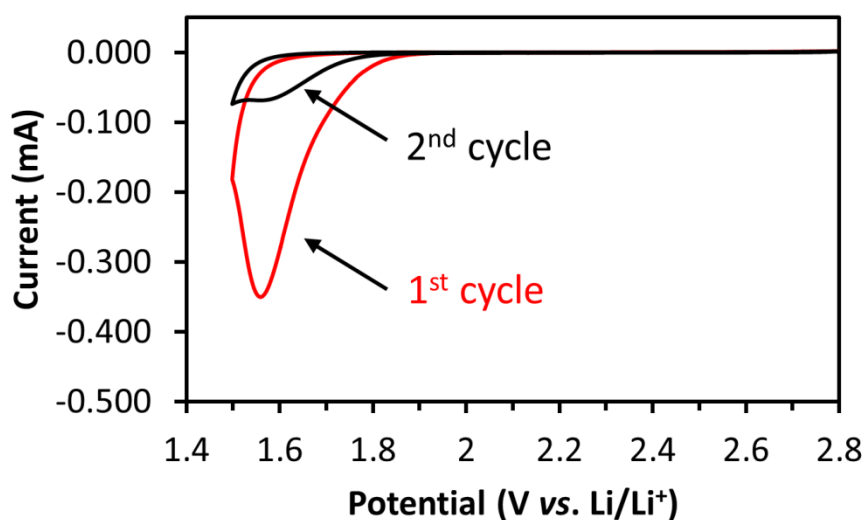


**Figure S23** CV curves of the blank cathode.

**Experimental Conditions:**

- 1 M LiTFSI in DOL/DME, 3% LiNO<sub>3</sub>
- Cathode area: **1 cm<sup>2</sup>**
- Scan rate: 0.1 mV/s
- Blank cathode: only carbon black and PVDF binder

LiNO<sub>3</sub> would be reduced irreversibly at potentials lower than 1.6V. We use the following experimental conditions to verify this conclusion. The blank cathode is prepared by using only carbon black and PVDF binder. As shown in **Figure S23**, a large cathodic peak at about 1.55 V is observed in the first cycle, which corresponds to LiNO<sub>3</sub> reduction. However, for the second cycle, the cathodic peak is diminished and the negligible peak current is observed, demonstrating that this reaction is irreversible and LiNO<sub>3</sub> reduction only happens in the first cycle.

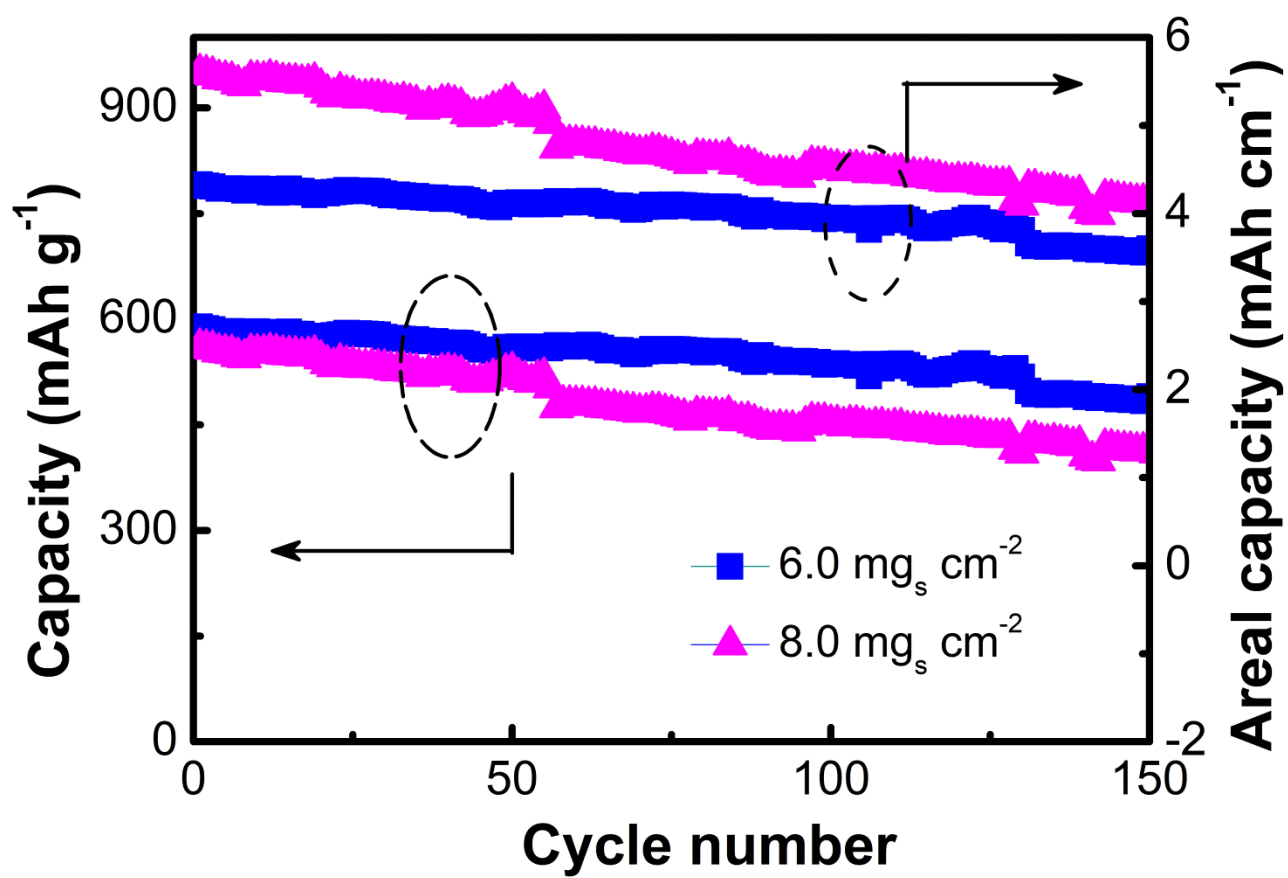


**Figure S24** Cycling performance of the *h*-Co<sub>4</sub>N@NC/S composite with sulfur loading of 6 and 8 mg<sub>s</sub> cm<sup>-2</sup>.